REGULAR PAPER

Methodology for shape prediction and conversion of a conventional aerofoil to an inflatable baffled aerofoil

S.R. Mistri[1], C.S. Yerramalli[1], R.S. Pant[1] and A. Guha[2]

[1]Department of Aerospace Engineering, Indian Institute of Technology Bombay, Mumbai, Maharashtra, India and [2]Department of Mechanical Engineering, Indian Institute of Technology Bombay, Mumbai, Maharashtra, India
Corresponding author: S.R. Mistri; Email: sohrab.mistri@iitb.ac.in

Abstract

Inflatable wings for UAVs are useful where storage space is a severe constraint. Literature in the field of inflatable wings often assumes an inflated aerofoil shape for various analyses. However, the flexible inflatable aerofoil fabric might deform to another equilibrium shape upon inflation. Hence accurate shape prediction of the inflated aerofoil is vital. Further, no standardised nomenclature or a process to convert a smooth aerofoil into its corresponding inflatable aerofoil counterpart is available. This paper analytically predicts the equilibrium shape of any inflatable aerofoil and validates the analytical prediction using non-linear finite element methods. Further, a scheme for the generation of two types of inflatable aerofoils is presented. Parameters such as the number and position of compartments and aerofoil length ratio (ALR) are identified as necessary to define the aerofoil's shape fully. A process to minimise the deviation of the inflatable aerofoil from its original smooth aerofoil using particle swarm optimisation (PSO) is discussed. Research presented in this paper can help in performing various analyses on the actual equilibrium shape of the aerofoil.

Nomenclature

ACR	area change ratio
ALR	aerofoil length ratio
$Area_{if}$	cross-sectional area of the inflatable aerofoil
$Area_{of}$	cross-sectional area of the original aerofoil
CFD	computational fluid dynamics
C_x	coordinate of circle centre along x direction
C_y	coordinate of circle centre along y direction
E	Young's modulus
FEA	finite element analysis
F_x	X component of the resultant force (N)
F_y	Y component of the resultant force (N)
GA	genetic algorithms
$J(x)$	objective function dependent on variable vector, x
lb	lower bound of a variable in the optimisation framework
n	number of independent variables (for optimisation framework)
P	internal pressure of baffles (N/m^2)
PSO	particle swarm optimisation
Q	angle of relevant component
r	radius
SA	simulated annealing

SD	standard deviation
t	fabric thickness
T	force (N)
ub	upper bound of a variable in the optimisation framework
x_i	coordinates of a point 'i' in x direction
y_i	coordinates of a point 'i' in y direction
∂x	infinitesimal distance in x axis
∂y	infinitesimal distance in y axis
$\emptyset$	angle of the relevant component
σ_{hoop}	hoop stress
ϵ	strain due to hoop stress

1.0 Introduction

Inflatable wings on UAVs are useful where storage space is a severe constraint. A typical example of such a scenario is an on-field soldier who needs to deploy a backpack carry-able unmanned aerial vehicle (UAV) for local area surveillance. Inflatable wings use air beams as their structural backbone, which form the aerofoil shape. The air beams can be circular while joined by an open cell foam structure, or the aerofoil itself can be built of multiple compartments along the wingspan. These systems are either inflated in flight or on the ground.

Right from their appearance in the mid-1930s, inflatable wings have been of interest to UAV designers and a topic of research. McDaniel's glider (1930) is one of the earliest records of inflatable wings [1], which consisted of tubular spars as the structural element. The inflatable wings were warped to establish roll control. Later in 1956, the Goodyear *Inflatoplane* was designed with the intention of recovering surviving pilots behind enemy lines [2, 3]. In 1970, the first UAV utilising inflatable wing technology named *Apteron* was designed [4]. The aim was to design an aircraft that can be stored in a low form factor and can be launched easily in remote locations. In 2002, the I-2000 was launched, which was a UAV with inflatable wings designed at the NASA Dryden Flight Research Centre. The purpose of the I-2000 was to study the flight characteristics of inflatable wings compared to fixed wings [5]. Since 2002, the BIG BLUE project was initiated as a joint effort with the University of Kentucky and NASA. Between 2002 to 2007, five versions of the inflatable winged UAV were developed [6], one of the primary goals was to check the feasibility of UV cured/hardened wings [7]. Inflatable wings have also been used for various gun launched UAV's, some of which include Forward Air Support Munition (FASM), Quicklook, and Gun Launched Observation Vehicle (GLOV) [8, 9].

The research on inflatable wings can be classified into a study of several sub-topics, e.g., structures, inflatable material identification, morphing, aerodynamics and subsystems such as inflation mechanism. Initially, Webber [10] studied the loading effects on a single air beam. Jun-Tao et al. [11] covers the theoretical concepts for structural strength of air beams and practical testing on NACA 0012 in its inflatable wing form. Walker et al. [12] and Murray et al. [5] have conducted practical load testing of an inflatable wing. Breuer et al. [13] have introduced the concept of tenacity by installing metal wires that run along the air beams, thus providing additional support and reducing the requirement of pressure from the inflation system. Usui et al. [14] and Fulcher et al. [15] have investigated the stress acting on an inflatable wing due to the internal pressure and the lifting force using finite element methods. With regards to research in the field of materials, a curable wing is a sought-after attribute. Cadogan et al. [16] have expanded on various curing techniques such as thermally cured thermoset composites, ultraviolet cured composites, inflation gas reaction composites and second order transition change and shape memory polymer (SMP) composites. Consistent efforts have been made to develop light/ UV curing inflatable wings to reduce the disadvantages of leakages [17–19]. Another successful deployment of the rigid inflatable wing is the BIG BLUE project [7]. In the sub-topic of aerodynamics, LeBeau et al. [20] and Krofta et al. [21] have performed a numerical comparison of flow over bumpy inflatable aerofoils. Simpson et al. [22, 23] conducted wind tunnel tests of inflatable wings to quantify their lift and drag
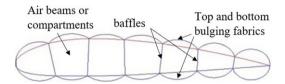
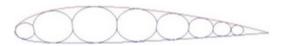**Figure 1.** *Externally baffled aAerofoil.*

Figure 2. *Internally baffled aerofoil.*

characteristics. In the field of aerofoil shape prediction, Marzocca et al. [24] have attempted to predict the equilibrium shape of the inflatable aerofoil by balancing the internal pressure against the membrane stress. However, the resultant shape prediction is not in equilibrium as, in certain cases, the top and bottom fabric arcs do not have the same circle centre coordinates. Further, they have attempted to minimise the deviation of the inflatable aerofoil from the original aerofoil. This concept was further developed in 2017 [25], to create a pareto front of the decrease in mass of the aerofoil against the penalty of aerofoil shape deviation from its original aerofoil. With regards to aerofoil shape validation, a critical review of literature related to the design of inflatable wing UAVs reveals a lack of a validated shape prediction model of the inflatable aerofoil. While, indeed, earlier research has assumed the shape of the inflatable aerofoil to be a series of intersecting circles [2, 4, 26–30], other work has assumed otherwise [11, 29, 31]. This paper addresses a major lacuna in the literature on inflatable wings by proving the shape of the inflatable aerofoil to be a series of intersecting circles and validates the same using a non-linear finite element analysis (FEA). Further, our work attempts to minimise the deviation of the shape of the inflated aerofoil from the original smooth aerofoil using particle swarm optimisation (PSO). PSO, a non-traditional optimisation technique is chosen since the nature of the objective function space is unknown.

We begin with a geometric shape identification of a single air beam that is composed of two baffles and two bulging fabric members at the top and bottom (refer Fig. 1). The inflatable aerofoil is classified into two types – externally baffled and internally baffled. An aerofoil where each baffle intersects the top and bottom sections of the original aerofoil (Fig. 1) has been termed externally baffled. The aerofoils where the bumps of the aerofoil are tangential to the original aerofoil (Fig. 2) have been termed internally baffled. Further, a standardised method to convert a conventional aerofoil into an inflatable aerofoil is presented. An example of the implementation of this approach is also presented. A formal procedure is proposed, using first principles, to derive the inflated shape of the fabric. This approach allows estimation of the shape deviation of the inflated fabric aerofoil from the regular shape of a conventional desired aerofoil before its fabrication is taken up.

There are numerous possible arrangements of the internal baffles for an inflatable aerofoil. The position and number of the baffles/compartments have a large bearing on the shape of the inflated aerofoil and its deviation from the conventional aerofoil. However, none of the previous work in this field specifies the position of these baffles; it is seen that they are generally equally or arbitrarily spaced. Hence, this paper further attempts to optimise the position of these baffles to minimise the geometric deviation of the inflated aerofoil to the original aerofoil.

Thus, this approach would help a designer to choose the number of baffles and as well as study the role of various aerofoil parameters on the shape deviation between inflated aerofoil and the conventional aerofoil.
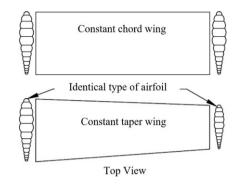
Figure 3. *Assumed wing shape to reduce problem dimensionality.*

2.0 Modelling methodology

An aircraft wing has a chordwise dimension, thickness dimension and a spanwise dimension. Ideally the inflatable wing geometry modelling could be treated as a three-dimensional problem. However, some practical considerations could be applied to reduce the problem from three dimensions to two dimensions. Similarly, the shape prediction of the inflatable aerofoil is restricted only to the ground-inflated static state. As this is the baseline inflated shape that the fabric aerofoil would attain upon inflation, aeroelastic modelling considerations are ignored.

2.1 Reduction of problem dimensionality

(1) The planform of the wing is assumed to be of constant chord or constant taper ratio (refer Fig. 3).
(2) The aerofoil at the root and tip are the same.
(3) The aspect ratio is assumed to be large.

2.2 Large deformation infinitesimal elastic deformation modelling

The fabric reaches its inflated shape from its original deflated state when internally pressurised. This deformation is being referred to as large body deformation. Further, the internal pressure would also cause an elastic deformation due to the tensile hoop stress generated in the fabric. This elastic deformation is considered to be negligible in the analytical derivation. This assumption is validated in the FEA analysis as mentioned in Section 7.2. Hence, this is treated as a large body deformation and small elastic deformation problem. This consideration permits the prediction of the final aerofoil independent of the material property system. Further, Section 3 proves that the large body deformations are independent of the internal pressure and material properties. This allows the results to be generalised to a large variety of fabrics.

3.0 Analytical inflated profile derivation

The inflated aerofoil shape is typically obtained by inflating a fabric that is cut and stitched in the shape of an aerofoil. During the inflation process, the upper and lower fabrics of the aerofoil will deform to create an outward bulge as well as some stretch in the fabric due to the internal pressure. In this analysis, the change in length of the fabric is ignored while predicting the shape of the inflated fabric. Initially, Subsection 3.1 analytically proves that the top and bottom fabrics naturally take the shape of an arc
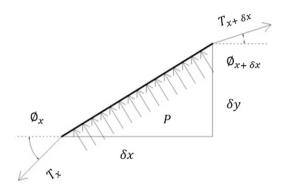
Figure 4. *Section of inflatable object fabric.*

under internal pressure. Subsections 3.2 proves that the top and bottom fabric arcs indeed have the same centre and radii for a specific case of unequal parallel baffles, while Subsection 3.3 proves the same for the most generic case of unequal titled baffles. The proofs mentioned in this section indicate that each compartment form a single circle, hence the entire aerofoil can be constructed as a series of intersecting circles.

3.1 Shape of the fabric under pressure

Consider an infinitesimal part of the inflated fabric of a bump on the aerofoil as shown in Fig. 4. Let the fabric have an out of plane thickness of 1 unit.

Balancing forces in the *x* and *y* direction:

$$-(T \cos \emptyset)_x + (T \cos \emptyset)_{x+\partial x} = P \times \partial y \tag{1}$$

$$-(T \sin \emptyset)_x + (T \sin \emptyset)_{x+\partial x} = -P \times \partial x \tag{2}$$

Equations (1) and (2) are derived under the assumption that the elastic deformation in the element is practically negligible. Converting Equations (1) and (2) into derivative form:

$$\frac{d(T \cos \emptyset)}{dx} = P \times \frac{\partial y}{\partial x} \tag{3}$$

$$\frac{d(T \sin \emptyset)}{dx} = -P \tag{4}$$

Integrating Equation (4)

$$T \sin \emptyset = -Px + Cnt_1 \text{ where } Cnt_1 \text{ is the constant of integration} \tag{5}$$

The origin is positioned as seen in Fig. 5. The *y*-axis cuts the fabric at point $(0, r)$. Hence replacing $x = 0$ and $\emptyset = 0$, the constant of integration equals 0. Rearranging Equation (5) gives: -

$$T = \frac{-Px}{\sin \emptyset} \tag{6}$$

Substituting *T* from Equation (6) in Equation (3):

$$\frac{d\left(-Px\frac{\cos \emptyset}{\sin \emptyset}\right)}{dx} = P \times \frac{\partial y}{\partial x} \tag{7}$$
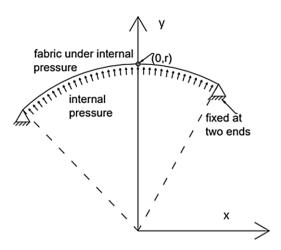
Figure 5. *Fabric under internal pressure.*

Since P is a constant and

$$\frac{\cos \emptyset}{\sin \emptyset} = \frac{1}{\tan \emptyset} = \frac{\partial x}{\partial y}$$

$$\frac{d}{dx}\left[x\frac{\partial x}{\partial y}\right] = -\frac{\partial y}{\partial x} \tag{8}$$

Upon integration and rearranging terms:

$$x\partial x = (-y + C_1)\,\partial y \tag{9}$$

Where C_1 is the constant of integration

Integrating Equation (9):

$$\frac{x^2}{2} + \frac{(y - C_1)^2}{2} = C_2 \tag{10}$$

Let $2C_2 = r^2$

Substituting (x, y) as $(0, r)$ and C_2 as r2/2 in Equation (9), it can be shown that $C_1 = 0$, hence

$$x^2 + y^2 = r^2 \tag{11}$$

This is the equation of a circle, hence it can be seen that a fabric held between two points always forms an arc of a circle. Further, it was found that the internal pressure does not play a role in the shape of the inflatable aerofoil under the assumption that the elastic deformation is negligible compared to the large body deformations. However, if this assumption is not considered, the fabric would undergo a constant elastic deformation based upon the quantum of internal pressure, the thickness of the fabric, and the material properties, while the shape of the top and bottom bulges would still remain circular arcs having the same centres and radii.

3.2 Unequal parallel baffles

The preceding section derived the shape of a fabric under internal pressure as an arc of a circle. The inflatable aerofoil is made of multiple compartments. Each compartment is composed of two straight baffles and two freely deformable upper and lower fabrics (Fig. 6). The position of the upper and lower circular fabric centres was introduced in our earlier work [32], which is elaborated here.
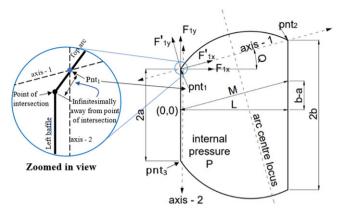
Figure 6. *Unequal parallel baffles.*

Since the fabric is flexible, it cannot resist any bending moment. However, once the fabric deforms to its natural equilibrium shape, the shape can be analysed as a rigid structure. Hence, if the forces are inspected along the cutting axes1- and axis-2 (Fig. 6), the reaction forces will not only balance in the horizontal and vertical components but also balance their moments. Further, pnt_1 is infinitesimally away from the point of intersection of the top arc and the left baffle as shown in the zoomed in view of Fig. 6, hence, the cutting axis (axis-2) in Fig. 6 is not at the baffle but within the compartment hence, only experiencing forces from within the concerned compartment rather than adjacent compartments.

Consider Fig. 6, taking moments and force balance along axes-1 and axis-2.

$$F_{1x} = +aP \tag{12}$$

$$F'_{1y} = P \times \frac{M}{2} \tag{13}$$

A detailed derivation of Equations (12) and (13) is given in Appendix A.

The tension force in the top arc fabric at pnt_1 can be resolved into a system of any two perpendicular forces. Hence, the same can be resolved either into (F_{1x}, F_{1y}) or (F'_{1x}, F'_{1y}). F'_{1y} can be written in terms of F_{1x} and F_{1y} as:

$$F'_{1y} = F_{1y} \cos Q - F_{1x} \sin Q \tag{14}$$

Substituting Equation (13) in (14):

$$P \times \frac{M}{2} = F_{1y} \frac{L}{M} - F_{1x} \frac{b-a}{M} \tag{15}$$

Rearranging Equation (15), substituting M as $\sqrt{L^2 + (b-a)^2}$ and reducing, we get

$$F_{1y} = \left(\frac{L^2 + b^2 - a^2}{2L} \right) \times P \tag{16}$$

Since the fabric cannot undergo any bending moment, the direction of the resultant force at pnt1 is along the tangent of the fabric at pnt1. Hence:

$$\left. \frac{d}{dx} \right|_{pnt1} = \frac{F_{1y}}{F_{1x}} = \frac{L^2 + b^2 - a^2}{2La} \tag{17}$$

The arc centre coordinates are of interest. The differential equation of a circle is:

$$(x - C_x) + (y - C_y) \times \frac{dy}{dx} = 0 \tag{18}$$

Replacing Equation (17) in (18), substituting (x, y) by $(0, a)$ and rearranging:

$$C_x = (a - C_y) \times \left(\frac{L^2 + b^2 - a^2}{2La} \right) \tag{19}$$

Equation (19) is one of the equations in terms of C_x and C_y. The second equation is derived from the arc centre locus line as shown in Fig. 6. The locus is the perpendicular bisector of the line joining pnt1 and pnt2. Hence writing the locus equation in the form of $y = mx + c$:

$$C_y = \left(\frac{L}{a - b} \times C_x \right) + \left(\frac{L^2 + b^2 - a^2}{2(b - a)} \right) \tag{20}$$

Rearranging Equation (20):

$$C_x = \left(\frac{a - b}{L} \times C_y \right) + \left(\frac{L^2 + b^2 - a^2}{2L} \right) \tag{21}$$

Solving Equations (19) and (21) together and rearranging:

$$\left(\frac{L^2 + b^2 - a^2}{2L} \right) - C_y \left(\frac{L^2 + b^2 - a^2}{2La} + \frac{a - b}{L} \right) = \left(\frac{L^2 + b^2 - a^2}{2L} \right) \tag{22}$$

Solving Equation (22) gives the value of C_y. Substituting the value of C_y in Equation (21) yields the value of C_x as follows:

$$C_y = 0, \; C_x = \left(\frac{L^2 + b^2 - a^2}{2L} \right) \tag{23}$$

Since $C_y = 0$, due to horizontal symmetry as seen in Fig. 6, the top and bottom fabrics share the same centre.

3.3 Unequally tilted baffles

The earlier section derived the position for the circle centre coordinates for a specific case of unequally parallel baffles. This section addresses a generic case of unequal tilted baffles as seen in Fig. 7(a). A geometrical approach to derive the location of the centre is implemented. The cutting lines labelled p and r are intestinally positioned inside the compartment rather than being exactly on the baffle. Hence the force balance on the baffles would only consider the concerned compartment and no adjacent compartment.

Consider reorienting Fig. 7(a) such that cutting line p is horizontal as shown in Fig. 7(b). To keep element a in balance Fig. 7(b), the horizontal forces, F_x must be equal and opposite. The vertical forces, F_y must be equal in magnitude and have the same direction to counteract the pressure P acting internally.

This implies that the resultant forces at the two end nodes of element a are equal and mirrored about the perpendicular bisector. Since the fabric cannot resist bending loads, the slope of the fabric or the derivative is Fy/Fx. Hence the centres of the side arcs as seen in Fig. 7(b) are mirrored along the perpendicular bisector.

The same can be said for both baffles and the other two dotted sides as shown in Fig. 8. The only way for the centres of the top and bottom fabrics to be mirrored in all four perpendicular bisectors is for all four perpendicular bisectors to intersect at one point. This point represents the circle centre coordinates of the top and bottom fabrics. Thus, each compartment has a circular cross section and can be thought of as an air beam in 3D.

Since each compartment is forming a single circle, the entire structure can be created as a combination of intersecting circles that form the shape of the bumpy aerofoil. The points where the circles intersect determine the location of the baffles. The bumps result in a deviation of shape from the original aerofoil. A parameter to quantify the deviation of the inflatable aerofoil to its conventional aerofoil is needed. This is introduced as the area change ratio (ACR), which is defined as the ratio of the change in the cross-sectional area of the inflatable aerofoil due to the conversion process to the cross-sectional area of the conventional aerofoil. The area refers to the cross-sectional area of the aerofoil as seen. ACR can only
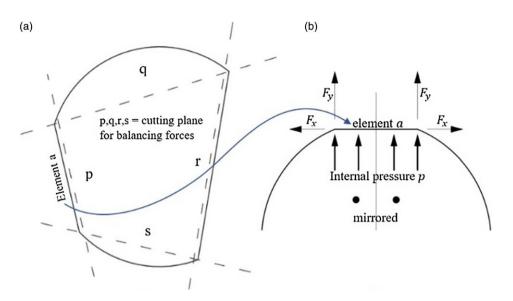
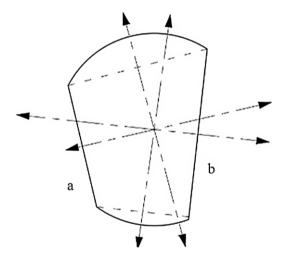**Figure 7.** *Unequal tilted baffles.*

Figure 8. *Unequal baffles.*

be used to quantify the deviation of a particular inflatable aerofoil configuration and cannot be used to specify the size of an aerofoil as the same inflatable version of a conventional aerofoil would have different ACR's depending on the number of compartments and locations of the baffles/ compartment centres.

$$ACR = \frac{\left|Area_{if} - Area_{of}\right|}{Area_{of}} \tag{24}$$

Where $Area_{if}$ is the cross-sectional area of the inflatable aerofoil and $Area_{of}$ is the cross-sectional area of the original aerofoil.

The shape of a single air beam has been derived in this Section. The next Section outlines a method to create an aerofoil by joining multiple air beams.

Table 1. *Parameter details of inflatable wings*

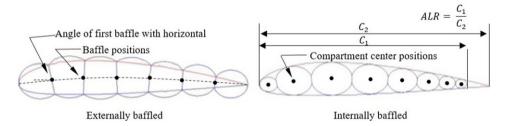| Parameter and description	Type of parameter	
	Internally baffled	Externally baffled
Aerofoil length ratio (ALR): The ratio of the chord of the inflatable aerofoil to the chord of the original smooth aerofoil.	Variable	Always unity
Angle of the first baffle: The angle the first baffle makes with the horizontal axis.	Dependent	Variable
Compartment Centre position: The horizontal position of the compartment centres. The vertical position and radii are fixed based on the type of aerofoil.	Variable	Dependent
Baffle position: The horizontal position of the intersection points of the baffles with the camber line.	Dependent	Variable

Figure 9. *Parameters of inflatable aerofoils.*

3.4 Parameters of inflatable wings

As derived in Section 3.3, an inflatable aerofoil can be designed as a series of intersecting circles. Two types of inflatable aerofoils are realised, externally baffled and internally baffled, as described in Section 1 through Figs. 1 and 2. Due to the nature of these two types of aerofoils, different parameters are either constant, variable or driven, depending on the type of inflatable aerofoils. This section familiarises the reader with these variables before introducing the method to develop the two types of inflatable aerofoils in subsequent Sections 4 and 6. Table 1 discusses the details of these parameters, while Fig. 9 depicts the same pictorially.

4.0 Externally baffled aerofoil generation algorithm

An overview of the algorithm designed to create the externally baffled aerofoil is shown in Fig. 10. Although the process for converting a symmetrical aerofoil is intuitive, the process for converting an unsymmetrical aerofoil is not and requires a formalisation of the process. The step-by-step process to convert any aerofoil (symmetric or un-symmetric) to an externally baffled aerofoil is given in Appendix C.

4.1 Outputs

An example of the output generated for NACA 4318 aerofoil with 20 compartments is shown in Fig. 11.

The change in the ACR as the number of compartments increases is shown in Fig. 12. The increase in area reduces as the number of compartments increases. Beyond 20 compartments, the value of ACR
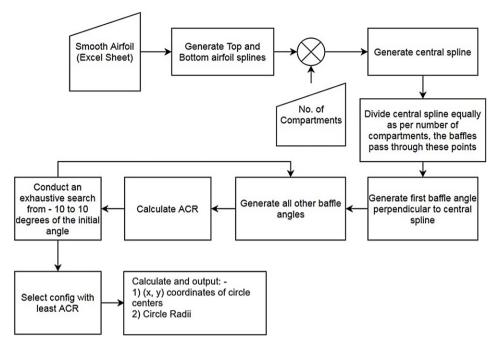
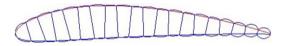*Figure 10. Flowchart for conversion of conventional to inflatable aerofoil.*

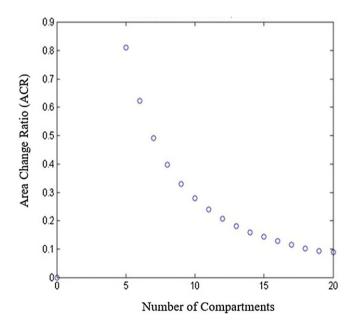*Figure 11. Bumpy aerofoil with 20 compartments.*

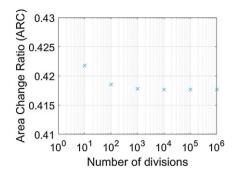*Figure 12. ACR vs number of compartments.*

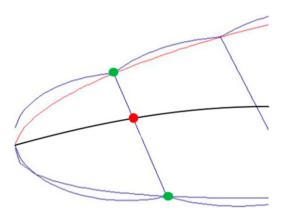***Figure 13.*** *ACR v/s number of divisions.*

Figure 14. *Baffle intersection points.*

settles to about 0.1. The user can utilise this information for further analysis, or to calculate the lengths of the fabric needed for the upper and lower bulging fabrics and the baffles during manufacturing.

4.2 Sensitivity test for allowed residues in iterative procedures

The baffle aerofoil generator algorithm had certain sections of the code which used iterative procedures. The sensitivity of the allowed residue of these processes is discussed below. The NACA 4318 with eight compartments is used for all the reported sensitivity test.

Area change ratio: The ACR has been defined as the increase in area of the bumpy aerofoil to its smooth aerofoil divided by the area of the smooth aerofoil. The area of the aerofoil is calculated through a numerical integration which involves an iterative procedure. The effect of the number of segments the chord is divided into on the ACR is seen in Fig. 13. It is seen that beyond ten thousand divisions, the change in ACR is negligible.

Finding baffle intersection points with the smooth aerofoil: As seen in Fig. 14, the centre red dot indicates the fixed centre of the baffle. The two outer intersection dots as seen in Fig. 14 need to be calculated. The first baffle angle and centre are fixed, and the intersection points are iteratively acquired. Once the first baffle is fixed, the subsequent baffle endpoints are iteratively calculated while keeping their centre fixed and varying their angle such that the earlier baffle intersection points and current points circumscribe a circle. A suitable termination criterion for the iterative procedures was found to be 10^{-4} for a unit chord as seen in Fig. 15.
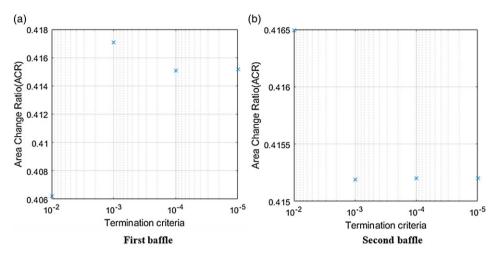
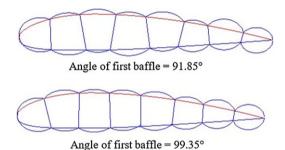**Figure 15.** *Termination criteria for first and second baffle calculations.*

Angle of first baffle = 91.85°

Angle of first baffle = 99.35°

Figure 16. *NACA 4318, 8 compartments, different angle of first baffle.*

5.0 ACR Minimisation by varying the first baffle angle

For a particular number of baffles, the angle of the first baffle determines the angles of all the subsequent baffles. Change in angle of the first baffle results in a change in orientation of all the other baffles and changes the ACR. An algorithm was developed to minimise the ACR by changing the angle of the first baffle. Figure 16 shows two different configurations for the same baseline specifications (NACA 4318) with eight equally spaced compartments.

Figure 17 shows the change in ACR as the angle of the first baffle increases. While a clear trend is visible, the magnitude of change of ACR is quite small. The red line indicates the angle at which the first baffle is vertical to the central spline of the aerofoil.

The process to create an externally baffled aerofoil has been discussed, the next section deals with creation of an internally baffled aerofoil.

6.0 Internally baffled aerofoil generation algorithm

The creation of equally spaced externally baffled aerofoils was presented in Section 3.4. In this section the process to generate internally baffled aerofoil is described. An overview of the algorithm designed to create the internally baffled aerofoil is shown in Fig. 18. The detailed method to create an internally baffled inflatable aerofoil is given in Appendix D.
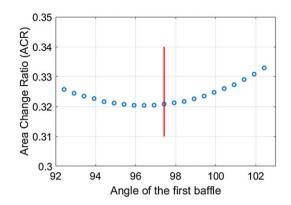
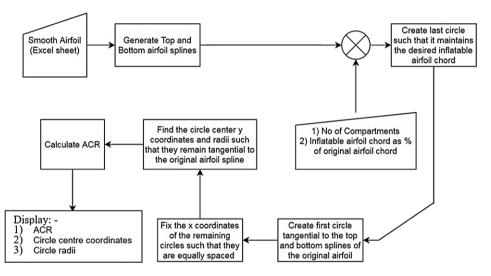**Figure 17.** *Increase in ACR vs angle of first baffle.*

Figure 18. *Flowchart for conversion of conventional to inflatable aerofoil.*
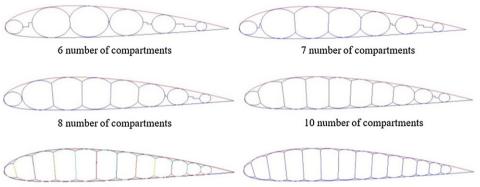
6.1 Output

Figure 19 shows the effect of varying the number of compartments for a NACA 4318 aerofoil. The chord of the inflatable aerofoil is 90% of the original aerofoil. The first circle centre *x*-coordinate is at 4% of original aerofoil chord length. The cases of equally spaced baffles, having compartments numbers ranging 6–10 have a gap between the circles, and these are infeasible solutions.

A Matlab® code has been written (and is available for distribution [33]) to generate either an externally baffled inflatable aerofoil, or internally baffled inflatable aerofoil from any four-digit NACA aerofoil. The user can specify parameters such as number of compartments and ALR. The code outputs necessary data like all compartment centre coordinates and radii, all baffle, upper fabric and lower fabrics lengths. These details can help users during the designing/ analysing and manufacturing process, etc.

7.0 Validation of analytical shape prediction model of an inflated aerofoil

The analytical solution predicts the shape of the top and bottom fabrics of the aerofoils to develop circular bulges having the same centres while the baffles remain straight. Hence, the entire aerofoil

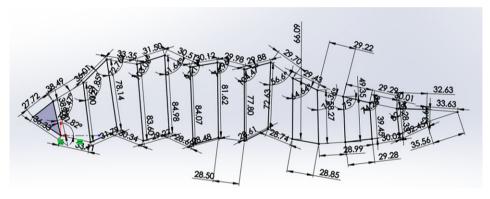**Figure 19.** *Internally baffled aerofoils before optimisation.*

Figure 20. *Initial pre-inflation shape for analysis.*

shape is predicted as a set of intersecting circles. Due to logistical restrictions, the authors have chosen to validate the analytically derived shape using non-linear FEA through Ansys. To ensure the simulation is independent of all assumptions and conclusions of the analytical shape prediction (Section 3), the initial geometry of all fabric segments are flat surfaces allowing the FEA solver to deform these fabric segments to their equilibrium shapes. The material chosen for the analysis is isotropic elastic Vectran, a material commonly used to make inflatable wings [4]. Relevant physical properties for Vectran are taken from Cadogan et al. [4]

7.1 Setup of NACA 4318 and NACA 8414, internally baffled aerofoils

The test case to validate the analytical shape prediction is the internally baffled aerofoil of NACA 4318, ALR 90% with 16 number of compartments and NACA 8414, ALR 85% with 16 number of compartments.

The setup of the problem is as follows:

Initial shape: The fabric is modelled as initially straight lines of appropriate length as seen in Fig. 20, which when inflated should take up the shape of interest. The same is created based on the above-mentioned aerofoils having original chord of 50cm. Although the initial state seems unnatural, the goal of this section is to show the final equilibrium shape of the aerofoil, hence the initial state can be any arbitrary geometry as long as the length of the fabric pieces are as per the analytical calculations.

Table 2. *Details of the problem setup in Ansys*

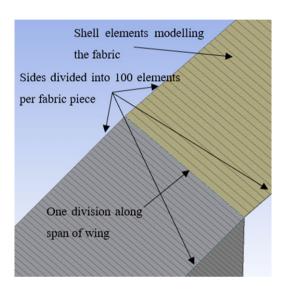| No.	Attribute	Description
1	Type of analysis	Static structural
2	Large body deformations	Active
3	Material	Vectran (properties taken from Cadogan et al. [4].)
4	Material thickness	50microns
5	Internal inflation pressure	10^5 Pa ($\sim$ 14.5PSI)
7	2D/3D	2D problem

Figure 21. *Element details of geometry.*

Physics of the problem: The physics of the problem are best described in Table 2.

Meshing: Only the 2D deflections are of interest for this validation case. Hence elements chosen are rectangular four-node, surface shell elements. The length of the fabric is divided into 100 divisions and only one division along the wingspan direction of the fabric is needed as seen in Fig. 21. The number of elements have been concluded to ensure mesh independence. Since the internal pressure is uniform along the spanwise direction, and loading conditions are non-varying along the span direction, no geometrical deviations are expected along the spanwise direction. Hence, choosing a single element in the span direction reduces the degrees of freedom hence improves simulation time.

Boundary conditions: Figure 22 indicates the boundary conditions. Internal pressure is applied in steps from 1 to 10^5Pa on all the upper and lower fabrics. Internal pressure has not been applied on the baffles as they experience the same pressure from both sides, hence the same cancels out. The junctions of the fabric are modelled with weak torsional stiffness. This is due to the geometry exhibiting a snap through behaviour if only revolute joints are used. The geometry tries to snap to the final shape which is predicted to be independent of internal pressure. Hence the weak spring helps to keep the system in equilibrium during the small internal pressure applications, while the weak spring stiffness becomes negligible as the internal pressure increases.

Final deformation: Figure 23 indicates the shape of the inflatable aerofoil from its initial shape to the final deformed shape. The sub figures of Fig. 23 are not meant to be compared as they denote the geometry deformation in FEA as the loading conditions are ramped. Figure 23(a) indicates the initial shape used for the simulation, Fig. 23(b) indicates a transitional shape while the static simulation is being performed while Fig. 23(c) and (d) indicate different views of the final shape of the FEA solution.
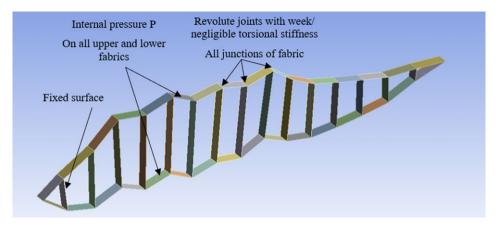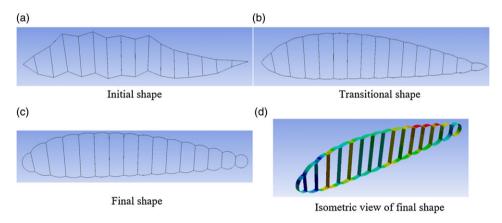
Figure 22. *Boundary conditions.*

Figure 23. *Initial, transitional, and final shape of NACA 4318.*

Analytical shape prediction validation using FEA solution: Figures 24 and 25 compares the FEA solutions to the analytical solution of the two inflatable aerofoil test cases. Figure 25 indicates the shape of NACA 4814 with 16 compartments, ALR of 85% while Fig. 24 indicates the shape of NACA 4318 with 16 compartments, ALR of 90%. No difference can be seen between the analytical and FEA solutions in both the cases. Hence the shape predicted by the FEA solution is in concurrence with the analytical shape prediction that the entire aerofoil inflates into a shape of a series of intersecting circles.

Although only two cases of internally baffled aerofoils have been validated in this section, externally baffled aerofoils are identical to internally baffled aerofoils in terms of the mathematics that govern their equilibrium shape of the flexible fabric upon inflation. The analytical model proves that a compartment will always have straight baffles and arc shaped top and bottom bulges having the same centre and radii, irrespective of the type of inflatable aerofoil, whether it be external or internally baffled.

7.2 Validation of strain-induced deformations

Figures 25 and 24 and captures the large body deformations; however, the strain induced elongation cannot be seen in the figure. Strained induced deformation will cause an increase in diameter for the circular compartments. The following derivation computes the analytical strain deformation in the largest
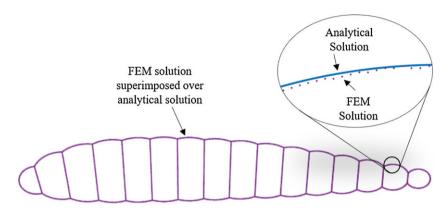
Figure 24. *Superimposed comparison of analytical and FEM shape prediction of NACA 4318 internally inflatable aerofoil, ALR 90%, 16 compartments.*
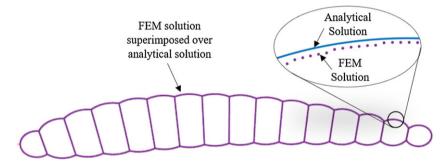

Figure 25. *Superimposed comparison of analytical and FEA shape prediction of NACA 4814 internally inflatable aerofoil, ALR 85%, 16 compartments.*

compartment for only the case shown in Fig. 24. Table 3 indicates the relevant material and geometric details:

The hoop stress is given as:

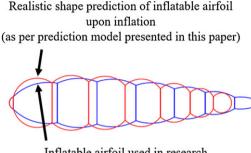$$\sigma_{hoop} = \frac{Pr}{t} = \sim 89.5 \text{Mpa} \tag{25}$$

Hence the strain due to the hoop stress is:

$$\epsilon = \frac{\sigma_{hoop}}{E} = 1.398 \times 10^{-3} \tag{26}$$

Hence the percent increase in diameter of the largest circular compartment due to strain would be ~0.14%. The same is negligible compared to the large body deformations hence cannot be seen in Fig. 24. The FEA solution gives a strain of 1.69×10^{-3}. This justifies the assumption that the tensile stress induced strain deformations are negligible compared to the large body distortions. Although the actual stress induced deformations would change depending on the material properties and the stress due to the internal pressure, the key contribution of the analytical model is to derive the natural equilibrium shape of the flexible fabric as opposed to assuming a shape as seen in the literature [11]. If the tension induced strain is not assumed to be negligible, the compartment top and bottom bumps would still take the shape of an arc, however with a slightly longer length/radius. The evaluation of the deformed lengths of the top and bottom arcs if the tension-based deformation is not negligible is derived in annexure II.

Table 3. *Material and geometric parameters for hoop stress calculation*

Parameter	Symbol	Value
Young's modulus	E	64 Gpa
Largest radius	r	44.75 mm
Material thickness	t	50microns

Realistic shape prediction of inflatable airfoil
upon inflation
(as per prediction model presented in this paper)

Inflatable airfoil used in research
by Jun-Tao et al.

Figure 26. *Difference between predicted and actual inflatable aerofoil shape [11].*

Section 3 has analytically proven the natural equilibrium shape of an inflatable aerofoil to be a series of intersecting circles, while Section 7 (current section) has validated the shape prediction using nonlinear FEA. An ideal example, to demonstrate the importance of the research presented in this paper can be seen in Fig. 26. The inflatable aerofoil geometry has been extracted from computation fluid dynamic (CFD) results presented in earlier research [11], where the shape of the inflatable aerofoil is assumed to be other than intersecting circles. Prediction or validation that the inflatable aerofoil would indeed take up the reported shape on inflation has not been discussed. As per aerofoil shape predictions presented in this paper, the actual geometry of the aerofoil taken up upon inflation completely changes as indicated in Fig. 26, hence rendering the CFD results invalid.

8.0 ACR Minimisation using independent movement of baffles

Sections 6 discussed the internally baffled aerofoil creation for equally spaced baffles. This section deals with further improving the ACR by changing the location of each baffle. Since the nature of the objective function space (ACR) is not known, there might be a single minimum or multiple local minima. Hence conventional optimisation algorithms such as steepest gradient descent was avoided and hybrid PSO, a stochastic optimisation algorithm was chosen. An inbuild function for hybrid PSO available in Matlab [34] is used. Hybrid PSO initially uses PSO to come to the global maxima region and then uses the steepest gradient method to arrive at the actual global minimum. The PSO algorithm is based on the work done by Kennedy and Eberhart [35] while incorporating modifications suggested by Mezura-Montes and Coello Coello [36] and Pedersen [37]. Since PSO is stochastic in nature, one needs to check for repeatability to ensure that the global minimum has been reached.

The following subsections describe the optimisation framework, comparison between PSO and hybrid PSO and finally the results.
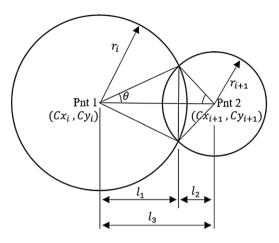
Figure 27. *Penalty function calculations.*

8.1 Optimisation framework

The objective is to minimise the ACR while enforcing a penalty function to ensure intersection of circles. The variables are the circle centre *x*-coordinates. The first compartment must be tangential to the front of the aerofoil and tangential to the aerofoil top and bottom splines, while the last compartment needs to be tangential to the vertical line governed by the aerofoil length ratio and the top and bottom aerofoil splines, hence, the first and last compartments are fixed in this optimisation study. Hence, the number of variables is equal to two less than number of compartments. The optimisation framework is stated in the equations below:

$$MinJ\,(Cx_{1ton}) = ACR + (Weightage \,^* \,Penalty\,function) \qquad (27)$$

Here,

$$\begin{aligned} Cx_{1ton} &= \text{circle centre} x - \text{coordinates} \\ n &= \text{number of independent parameters} = \text{number of compartments} - 2 \end{aligned} \qquad (28)$$

The penalty function is added to the objective function to ensure that consecutive compartments not only intersect but subtend a minimum defined angle θ as shown in Fig. 27.

The penalty function per adjacent compartment pair is the difference of the actual distance between adjacent compartment centres and the maximum allowable distance between the adjacent compartment centres. If the same is positive, the penalty function is considered else it is considered as zero. A detailed derivation of the penalty function formulation is given below. Figure 27 is given as an aid to this derivation.

The penalty function is defined based on a minimum angle θ as shown in the Fig. 27. Based on this angle, lengths l_1 and l_2. can be evaluated as:

$$l_1 = \max\,(r_i, r_{i+1}) \times (1 - \cos\theta) \qquad (29)$$

$$l_2 = \min(r_i, r_{i+1}) \times \left(1 - \cos\left(\sin^{-1}\frac{\max(r_i r_{i+1} \sin\theta)}{\min(r_i r_{i+1})}\right)\right)$$

Hence, the maximum allowable length between the centres can be evaluated as:

$$l_3 = l_1 + l_2 \qquad 30)$$

Table 4. *PSO parameters*

Sr.	Detail	Description
1	Initial population	Randomly uniformly distributed
2	Objective function tolerance	10-6 for only PSO, 10-6 for PSO plus steepest gradient, 10-8 also attempted for PSO plus steepest gradient
3	Max iterations	200 * no of variables = 3,000
4	Max stall iterations	20, number of iterations where global minima changes less than max function tolerance
5	Inertia range	Min 0.1Max 1.1
6	Self-adjustment weight (c1)	1.49
7	Social adjustment weight (c2)	1.49
8	Swarm size	Min (100, 10*number of variables)

The actual length between the centres is given by:

$$actual_{Length} = \left(\sqrt{(Cx_i - Cx_{i+1})^2 + (Cy_i - Cy_{i+1})^2} \right) \tag{31}$$

Hence the penalty for a consecutive compartment pair is given as:

$$penalty_i = \left(\sqrt{(Cx_i - Cx_{i+1})^2 + (Cy_i - Cy_{i+1})^2} - l_3 \right) \; if \; positive \tag{32}$$

$$= 0 \quad if \; negative$$

The final penalty function is given as

$$Penalty \, function = \sum_1^n (penalty_i)^2 \tag{33}$$

The constraint is:

$$-(Cx_i - Cx_{i+1}) \leq -(\min distance), \; i = 0 \; to \; (n-1) \tag{34}$$

Centre x-coordinates. This value is driven by the user and depends on the manufacturing capabilities available.

The PSO parameters chosen are given in Table 4.

8.2 Repeatability of hybrid PSO

The reliability of the PSO algorithm and hybrid PSO algorithm has been established by running it several times to check the repeatability of the results. Hybrid PSO has a higher computation time compared to normal PSO, hence one needs to check if the accuracy gained is worth the increased computation time. A NACA 4318 is converted to an internally baffled aerofoil having 17 compartments and an inflatable aerofoil to smooth aerofoil chord ratio as 0.9. The design variables for this repeatability test are the second compartment to second last compartment centre positions amounting to 15 design variables.

The improvements in the objective function (ACR) are given in Table 5.

PSO has improved the results by 3.7% and the (SD/mean) is negligible as shown in Table 5. Since the SD to average ratio is negligible, one can conclude that all the runs are converging to a single global minimum. The small variation of the design variables across multiple runs of the PSO indicate the repeatability of the optimisation algorithm. The variation of the design variables has been compared for the PSO and the hybrid PSO algorithm. One can compare the variance of the data. However, this will not give an indication of the span of the optimised variable value within its upper and lower

Table 5. *PSO results for 18 runs on internally baffled NACA 4318 having 17 compartments*

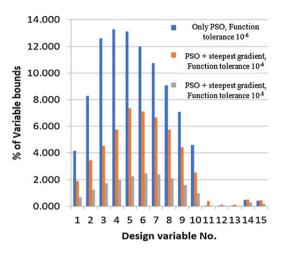| Average ACR	Min optimised ACR	Average fractional improvement	Best fraction improvement	SD	Standard deviation (SD)/average
0.03129	0.0312	0.03724	0.0373	2.24734E-06	7.18226E-05

Figure 28. *Optimised design variable range as a percent of variable bounds.*

bounds of each variable defined in the optimisation routine. Hence the following parameter has been compared:

$$\frac{(\max - \min)}{ub - lb}\%\qquad(35)$$

Where *ub* and *lb* refers to the upper bound and lower bound respectively, defined for each design variable (in this case being compartment centre positions) in this optimisation study. Since 18 identical runs have been performed, the max and min refers to the maximum position and minimum position of each design variable obtained across the 18 optimisation runs.

The $\frac{(\max - \min)}{ub - lb}\%$ for only PSO is maximum at 13.27%.

The $\frac{(\max - \min)}{ub - lb}\%$ for Hybrid PSO is maximum at 7.346%.

The $\frac{(\max - \min)}{ub - lb}\%$ for Hybrid PSO with objective function tolerance increased from 10^{-6} to 10^{-8} is maximum at 2.4%.

Thus, a hybrid optimisation such as PSO combined with the steepest gradient method has better repeatability in comparison to only PSO, as can be seen in Fig. 28.

8.3 Internal baffle results

The previous subsections have laid out the optimisation framework and validated the repeatability of the hybrid optimisation algorithm. This subsection illustrates the optimisation results for different number of compartments.

The optimisation algorithm has been implemented on compartment numbers ranging from 6 to 14. Fig. 29 illustrates the results.

Figure 29. *Visual comparison of inflatable aerofoil before and after optimisation.*

It is seen that compartment numbers below 10 are initially not feasible as all circles do not intersect. However, solutions for compartments 9 and 10 are feasible post optimisation. Solutions for compartment numbers 6 and 7 are still infeasible although the circles are now equally spaced due to the penalty function's effect in the objective function.

Figure 30 illustrates the movement of each baffle parametrised to the original aerofoil chord length post optimisation. A trend that is observed is, the circle towards the front of the aerofoil moves towards the leading edge while circles towards the aft of the aerofoil move towards the trailing edge. The movement of the first and last compartment are zero since they are kept fixed for this study.

Figure 31 shows the outcome of the optimisation framework. The ACR optimisation has been run on the NACA 4318 aerofoil for a range of compartment numbers from 11 to 20 as seen on the abscissa. The improvement in ACR post optimisation as a percent compared to the ACR of the baseline configuration is shown on the ordinate. The type of aerofoil created is internally baffled with the inflatable aerofoil to original aerofoil chord ratio as 0.90. A linear improvement in ACR is observed with an increase in the number of compartments. The improvements in ACR ranges from ∼2.75 to ∼7.25% for this study. From Fig. 31, it is also observed that the minimum improvement occurs when the number of compartments is 12. This is an extremely case-specific outcome. The number of compartments at which the improvement is minimum would be different for a different type of aerofoil. Thus, this result is not indicative of any fundamental property of inflatable aerofoils but has emerged by virtue of the geometry of the inflatable aerofoil being used in this specific study. The results would largely vary based on the geometries/aerofoils being studied.
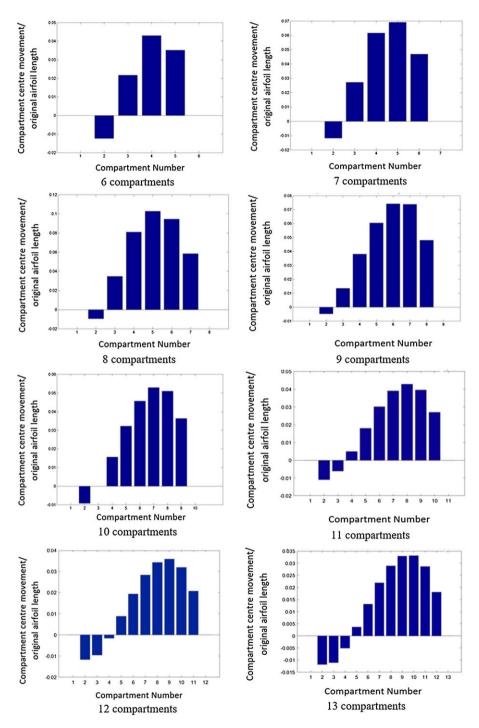
Figure 30. *Movement of each baffle parametrised to the original aerofoil chord length.*
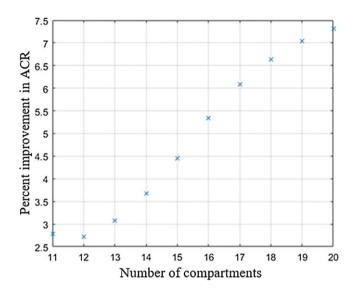
Figure 31. *Percent improvement in ACR for various number of baffles.*

Literature on inflatable wings indicates a purely empirical or trial/error approach to placing the baffles at various chord locations. This inevitably leads to a deviation of the shape from the smooth aerofoil that it was intended to mimic. No attempt has been reported on either quantifying or trying to minimise this deviation by developing a formal analytical approach to the design and placement of baffles. Our work is the first attempt in this direction. The ACR quantifies this deviation and the optimisation procedure reported in this work minimises it. The main contribution of the reported optimisation routine is not the quantum of improvement but an attempt to investigate an unanswered question of the literature: – can the deviation of the inflatable aerofoil from its original aerofoil be reduced by optimising the location of the baffles? The improvement in aerodynamic performance which may occur due to our proposed systematic method of baffled aerofoil construction and the consequent minimisation of the ACR, has not been quantified yet. This is a part of an ongoing investigation involving computational fluid dynamics and is outside the scope of this paper.

9.0 Conclusions

This study analytically proves the top and bottom fabrics of a single compartment of an inflatable aerofoil naturally deform to the shape of arcs having the same centres upon inflation. Hence, the shape of any baffled inflatable aerofoil is predicted to be a series of intersecting circles. The analytical shape prediction is validated using nonlinear FEA analysis, for two inflatable aerofoils each of 16 compartments, viz., NACA 4318 with ALR 90%, and NACA 8414 with ALR 85%. A perfect geometrical match between the analytical and FEA model was obtained. The analytical model assumes hoop stress induces strain deformations to be negligible for an isotropic linear elastic model of Vectran as its material. This assumption is validated through the FEA model, which indicates a maximum strain of 1.398×10^{-3}.

Further, the paper defines and standardises the conversion process to generate two types of aerofoils as internally baffled and externally baffled aerofoils from their original smooth aerofoils. Parameters that fully define the inflatable aerofoil are standardised as number and position of compartments, ALR and angle of the first baffle. The deviation of the inflatable aerofoil from its original smooth aerofoil is minimised using hybrid PSO. The objective function coined as ACR quantifies the area deviation between the inflatable aerofoil and original smooth aerofoil. Optimisation has been tested on an internally baffled inflatable NACA 4318 aerofoil with ALR 90% for number of compartments ranging from

11 to 20. The ACR improved by ∼2.8% for 11 number of compartments and increases with higher number of compartments. The ACR improvement was ∼7.3% for 20 number of compartments. The baffle centre positions were found to marginally vary from their base line positions post optimisation. For example, the maximum movement of a compartment centre was found to be 4% for NACA 4318 having 11 compartments. Hence manufacturing accuracies must be adequate to practically attain the desired improvements in ACR.

Current work has validated the inflated aerofoil shape prediction model using nonlinear FEA. Future work can included shape validation through practical testing using photogrammetry techniques. Apart from ACR, other parameters can be chosen as objective functions in the optimisation process. Hence, future work could include choosing parameters that have an impact in a multidisciplinary framework involving structures and aerodynamics. Parameters such as Cl/Cd and section modulus or strength to weight ratio can be used as objective functions. Literature [38] does indicate that a change in the surface properties can lead to significant changes in its aerodynamic properties of the inflatable aerofoil. These may show a greater improvement due to the optimisation exercise compared to the area change ratio.

References

[1] McDaniel, T.T. M'c Daniel Flying Machine, United States Patent Office Patent 1,905,298, 1933, 25th April 1933.

[2] Norris, R.K. and Pulliam, W.J. Historical perspective on inflatable wing structures, 50th AIAA/ASME/ASCE/AHS/ASC Structures, Structural Dynamics, and Materials Conference, Palm Springs, California, 2009, doi: 10.2514/6.2009-2145

[3] Winchester, J. *The World's Worst Aircraft: From Pioneering Failures to Multimillion Dollar Disasters*, Barnes & Noble Books, 2005.

[4] Cadogan, D., Graham, W. and Smith, T. Inflatable and rigidizable wing for unmanned aerial vehicles, 2nd AIAA "Unmanned Unlimited" Conference and Workshop & Exhibit, San Diego, California, 2003, doi: 10.2514/6.2003-6630

[5] Murray, E., Pahle, J., Thornton, S., Vogus, S., Frackowiak, T., Mello, J. and Norton, B. Ground and flight evaluation of a small-scale inflatable-winged aircraft, 40th AIAA Aerospace Sciences Meeting & Exhibit, Reno, Nevada, 2002, doi: 10.2514/6.2002-820

[6] Smith, S., Seigler, M., Smith, W. and Jacob, J. Multi-disciplinary multi-university design of a high-altitude inflatable-wing aircraft with systems engineering for aerospace workforce development, 46th AIAA Aerospace Sciences Meeting and Exhibit, Reno, Nevada, 2008, doi: 10.2514/6.2008-490

[7] Simpson, A., Rawashdeh, O., Smith, S., Jacob, J., Smith, W. and Lumpp, J. BIG BLUE: high-altitude UAV demonstrator of Mars airplane technology, 2005 IEEE Aerospace Conference, Big Sky, Montana, USA, 2005, doi: 10.1109/AERO.2005.1559753

[8] Brown, G., Haggard, R. and Norton, B. Inflatable structures for deployable wings, AIAA Aerodynamic Decelerator Systems Technology Conference and Seminar, Boston, 2001, doi: 10.2514/6.2001-2068

[9] Smith, T., McCoy, E., Krasinski, M., Limaye, S., Shook, L., Uhelsky, F. and Graham, W. Ballute and parachute decelerators for FASM/quicklook UAV, 17th AIAA Aerodynamic Decelerator Systems Technology Conference and Seminar, Monterey, California, 2003, doi: 10.2514/6.2003-2142

[10] Webber, J.P. Deflections of inflated cylindrical cantilever beams subjected to bending and torsion, Aeronaut. J., 1982, 86, (858), pp 306–312, doi: 10.1017/S000192400001914X

[11] Jun-Tao, Z., Zhong-xi, H. and Guo Zheng, C.L.-l. Analysis and flight test for small inflatable wing design, world academy of science, *Eng. Technol.*, 2012, **6**, (9), pp 1934–1939, doi: 10.5281/zenodo.1329184

[12] Scott, A. and Walker, J.I. Initial performance assessment of hybrid inflatable structures, *Acta Astronautica*, 2011, **68**, (7-8), pp 1185–1192, doi: 10.1016/j.actaastro.2010.10.009

[13] Breuer, J., Ockels, W. and Luchsinger, R.H. An inflatable wing using the principle of Tensairity, 48th AIAA/ASME/ASCE/AHS/ASC Structures, Structural Dynamics, and Materials Conference, Honolulu, Hawaii, 2007, doi: 10.2514/6.2007-2117

[14] Usui, M., Jacob, J., Smith, S. and Simpson, A. Development and flight testing of a UAV with inflatable-rigidizable wings, 42nd AIAA Aerospace Sciences Meeting and Exhibit, Reno, Nevada, 2004, doi: 10.2514/6.2004-1373

[15] Fulcher, J., Scherrer, I.J. and Suzanne, S.W. Using nonlinear FE modeling to understand the effect of boundary conditions on precise surfaces of inflatable structures, AIAA/ASME/ASCE/AHS/ASC Structures, Structural Dynamics, and Materials Conference, Boston, Massachusetts, 2013, doi: 10.2514/6.2013-1867

[16] Cadogan, D.P. and Scarborough, S.E. Rigidizable materials for use in gossamer space inflatable structures, 19th AIAA Applied Aerodynamics Conference, Anaheim, California, USA, 2001, doi: 10.2514/6.2001-1417

[17] Haight, A.H., Allred, R., Harrah, L., McElroy, P., Scarborough, S. and Smith, T. Design and fabrication of light rigidizable inflatable wings, 47th AIAA/ASME/ASCE/AHS/ASC Structures, Structural Dynamics, and Materials Conference, Newport, Rhode Island, 2006, doi: 10.2514/6.2006-1695

[18] Allred, R., Hoyt, A., Harrah, L., McElroy, P., Scarborough, S., Cadogan, D. and Pahle, J. Light curing rigidizable inflatable wing, 45th AIAA/ASME/ASCE/AHS/ASC Structures, Structural Dynamics & Materials Conference, Palm Springs, California, 2004, doi: 10.2514/6.2004-1809

[19] Allred, R., Hoyt, A., Harrah, L., Scarborough, S., Mackusick, M. and Smith, T. Light rigidizable inflatable wings for UAVs, 46th AIAA/ASME/ASCE/AHS/ASC Structures, Structural Dynamics and Materials Conference, Austin, Texas, 2005, doi: 10.2514/6.2005-1882

[20] LeBeau, R., Reasor, D., Gilliam, T., Schloemer, A., Hauser, T. and Johansen, T. Numerical comparison of flow over bumpy inflatable airfoils, 47th AIAA Aerospace Sciences Meeting including The New Horizons Forum and Aerospace Exposition, Orlando, Florida, 2009, doi: 10.2514/6.2009-1306

[21] Krofta, J., Spencer, G., Janiczek, M., Loiacono, R. and LeBeau, R.P. Analysis of aerodynamic flows over partially undulating airfoil surfaces, AIAA Scitech 2019 Forum, San Diego, California, 2019, doi: 10.2514/6.2019-2113

[22] Simpson, A., Santhanakrishnan, A., Jacob, J., Smith, S., Lumpp, J., Cadogan, D., Mackusick, M. and Scarborough, S. Flying on air: UAV flight testing with inflatable wing technology, AIAA 3rd "Unmanned Unlimited" Technical Conference, Workshop and Exhibit, Chicago, Illinois, 2004, doi: 10.2514/6.2004-6570

[23] Simpson, A., Jacob, J. and Smith, S. Flight control of a UAV with inflatable wings with wing warping, 24th AIAA Applied Aerodynamics Conference, San Francisco, California, 2006, doi: 10.2514/6.2006-2831

[24] Marzocca, P., Gurdal, Z., Hol, J., Chang, C., Crosbie, E. and Calder, T. Design and shape optimization of inflatable wings, 47th AIAA/ASME/ASCE/AHS/ASC Structures, Structural Dynamics, and Materials Conference, Newport, Rhode Island, 2006, doi: 10.2514/6.2006-1823

[25] Qingli, S. and Hua, W. Inflatable airfoil structure optimization on flying wing Buoyancy-lifting unmanned aerial vehicles, 2017 IEEE International Conference on Unmanned Systems (ICUS), Beijing, China, 2017, doi: 10.1109/ICUS.2017.8278350

[26] Cadogan, D., Smith, T., Uhelsky, F. and MacKusick, M. Morphing inflatable wing development for compact package unmanned aerial vehicles, 45TH AIAA/ASME/ASCE/AHS/ASC Structures, Structural Dynamics & Materials Conference, 2004, doi: 10.2514/6.2004-1807

[27] Rendall, T., Chang, C., Marzocca, P., Bollt, E. and Zamankhan, P. Aeroelastic behavior of a non-rigidizable inflatable UAV wing, 47th AIAA/ASME/ASCE/AHS/ASC Structures, Structural Dynamics, and Materials Conference, Newport, Rhode Island, 2006, doi: 10.2514/6.2006-2161

[28] Jacob, J. and Smith, S. Design of HALE aircraft using inflatable wings, 46th AIAA Aerospace Sciences Meeting and Exhibit, Reno, Nevada, 2008, doi: 10.2514/6.2008-167

[29] Jacob, J. and Smith, S. Design limitations of deployable wings for small low altitude UAVs, 47th AIAA Aerospace Sciences Meeting including The New Horizons Forum and Aerospace Exposition, Orlando, Florida, 2009, doi: 10.2514/6.2009-745

[30] Ben, L. and Jacob, J. In-flight deployment dynamics of inflatable wings, 48th AIAA Aerospace Sciences Meeting Including the New Horizons Forum and Aerospace Exposition, Orlando, Florida, 2010, doi: 10.2514/6.2010-54

[31] Booker, A., Fathepure, M., Nelsen, T., Tikalsky, D., Wang, N., Abouzahr, O., Cole, A., Kheong Loh, W. and Jacob, J.D. Conceptual design of an inflatable-winged aircraft for the exploration of Titan, AIAA Aviation 2020 Forum, Virtual Event, 2020, doi: 10.2514/6.2020-2786

[32] Kancherla, S.R., Dusane, C.R., Mistri, S.R. and Pant, R.S. Analytical modelling of baffled inflatable wing for failure prediction, AIAA Aviation 2019 Forum, Dallas, Texas, 2019, doi: 10.2514/6.2019-3366

[33] Mistri, S.R. 2021. [Online]. Available: https://github.com/sohrabmistri/-inflatable-airfoil-geometric.git [accessed 12 08 2021].

[34] The MathWorks Inc., MATLAB. version 9.9.0.1467703 (R2020b), Natick, Massachusetts, 2020.

[35] Kennedy, J. and Eberhart, R. Particle swarm optimization, Proceedings of the IEEE International Conference on Neural Networks, Perth, Australia, 1995, doi: 10.1109/ICNN.1995.488968

[36] Mezura-Montes, E. and Coello Coello, C.A. Constraint-handling in nature-inspired numerical optimization: Past, present and future, *Swarm Evol. Comput.*, 2011, **1**, (4), pp 173–194, doi: 10.1016/j.swevo.2011.10.001

[37] Pedersen, M.E.H. *Good Parameters for Particle Swarm Optimization*, Hvass Laboratories, 2010, Luxembourg.

[38] Johansen, T.A. Optimization of a Low Reynold's Number 2-D Inflatable Airfoil, Masters thesis, Utah State University, 2011.

Appendix A

This annexure details the derivations of Equations (12) and (13). Equations (12) and (13) are derived in conjunction with Fig. 6. The same figure is reproduced as Fig. A.1 for the ease of readers along with a zoomed-in view around pnt_1. Two details about pnt_1 are of vital importance: the point is on the
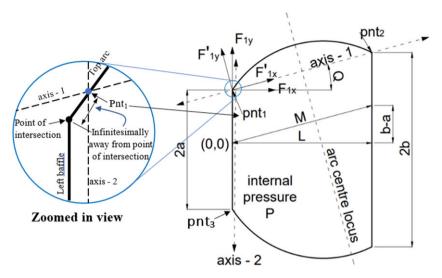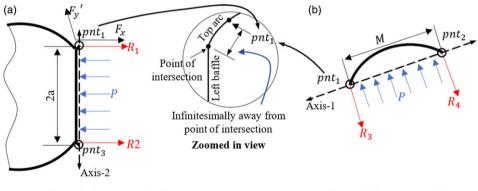
Figure A.1. *Unequal parallel baffles.*

Figure A.2. *Extracted view of left baffle and top bulge.*

top arc, and is infinitesimally away from the point of intersection as shown in the zoomed-in view in Fig. A.1. If pnt$_1$ was exactly at the point of intersection, forces from the compartment under consideration and the compartment to the left would be needed for the force balance equations. Pnt$_1$ being on the top arc, ensures that only forces within the compartment under consideration are needed for the force balance equations. It is of mathematical significance that pnt$_1$ is infinitesimally away from the point of intersection, since as this distance tends to zero, the tension forces within the top arc at pnt$_1$, would be the same tension force exerted by the top arc on the baffle at their point of intersection.

This derivation assumes an immediate change of shape from a linear baffle to an arc at the point of intersection. In reality, a minor fillet might be observed at the point of intersection based on the material property and thickness.

The tension force in the top arc fabric at *pnt*$_1$ as seen in the zoomed in view in Fig. A.1, can be resolved into a system of any two perpendicular forces. Hence, the same can be resolved either into $\left(F_{1x}, F_{1y}\right)$ or $\left(F'_{1x}, F'_{1y}\right)$.

The necessary components about axis-1 and axis-2 are extracted from Fig. A.2 and shown separately in Fig. A.2. Since pnt$_1$ is infinitesimally away from the point of intersection (marked in Figs A.1 and

A.2), the distance between pnt_1 and pnt_3 is considered as *2a* as shown Fig. A.2(a). Note that axis-2 is not inspecting the force balance of the left baffle only, but the aerofoil to the left of the axis-2 itself.

While drawing attention to the cutting axis-2 in Fig. A.2(a), *P* is the uniform internal pressure where the fabric is considered to have a width of unity coming out of the paper. R_1 and R_2 are the reaction forces that keep the baffle in static equilibrium.

Balancing the forces for the left baffle:

$$R_1 + R_2 = P \times 2a \tag{A1}$$

Balancing the moments at pnt_1 of the left baffle:

$$\underset{(Force\ due\ to\ uniform\ pressure)}{(P \times 2a)} \times \underset{(Moment\ arm\ of\ force)}{(a)} = R_2 \times (2a) \tag{A2}$$

Evaluating R_2 from Equation (A2), and substituting the value of R_2 into Equation (A1) to get R_1:

$$R_1 = R_2 = Pa \tag{A3}$$

The reaction force R_1 in Fig. A.2 is denoted by F_{1x} in Fig. A.1. Since they are same, Equation (12) is obtained as:

$$F_{1x} = R_1 = Pa \tag{A4}$$

Similar to the derivation process stated for evaluation of R_1 and R_2, R_3 and R_4 in Fig. A.2(b) can be evaluated as:

$$R_3 = R_4 = P \times \frac{M}{2} \tag{A5}$$

Since the reaction force exerted on the top arc at pnt_1 is R_3, an equal and opposite force will be exerted at pnt_1 of the left baffle. This equal and opposite force is denoted by F'_{1y} in Fig. A.1, hence giving rise to the equation below. Note that the F'_{1y} is in the opposite direction as R_3 hence the magnitude is not negative as this is taken care of in the direction of F'_{1y}. The following equation is identical to Equation (13).

$$F'_{1y} = R_3 = P \times \frac{M}{2} \tag{A6}$$

Appendix B

This annexure evaluates the strain the fabric of the inflatable aerofoil if the tension-induced deformation is not negligible. Figure B.1 shows a compartment of an inflatable aerofoil. The stress in the fabric can be evaluated using hoops stress formulation, denoted by σ. The pre-inflation diameter of the compartment is denoted as d_i. Upon inflation under pressure *P*, as shown in Fig. B.1, the diameter post extension of the compartment is denoted as d_f.

Since the length of the top and bottom arcs, are directly proportional to the circumference of the compartment, which in turn is directional proportional to the diameter of the compartment, although the strain is physically noticed in the fabric material, one can form the stress strain relation as:

$$\sigma = \epsilon E \tag{B1}$$

Where *E* is the Young's modulus of the fabric material and is the strain.

As per hoops stress formulation:

$$\sigma = \frac{P}{2t} \times d_f = \frac{P}{2t} \times ((1 + \epsilon)d_i) \tag{B2}$$

Combining Equations (C9) and (C10):

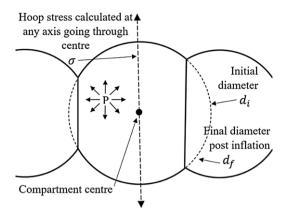$$\epsilon E = \frac{P}{2t} \times ((1 + \epsilon)d_i) \tag{B3}$$

Figure B.1. *Strain evaluation in the fabric.*

Rearranging to evaluate μ:

$$\epsilon = \frac{P \times d_i}{2Et - Pd_i} \tag{B4}$$

Hence if L_i is the original length of the top or bottom arc, and L_f is the deformed length of the respective arc:

$$L_f = (1 + \epsilon) \times L_i \tag{B5}$$

Appendix C

This appendix discusses the procedure to generate an externally baffled inflatable aerofoil.

Inputs

The user needs to specify the coordinate points of the smooth aerofoil in the form of a spreadsheet, or a text file. The user can also give the NACA four-digit series number and the code will create the smooth aerofoil coordinates itself. Once the smooth aerofoil coordinates are given, the user needs to give the number of compartments needed to create the inflatable aerofoil.

Converting inputs to code requirements

First, the coordinates are used to generate the upper and lower splines of the smooth aerofoil. The central spline is generated, and the coordinates of the points equally spaced along the x-axis as per given number of compartments are calculated. The baffles will pass through these points on the central spline. For a particular angle of one of the baffles, the angles of all other baffles need to be calculated so that the inflatable conforms to the shape of the original aerofoil.

Finding baffle intersection points with the smooth aerofoil

One way to calculate the intersection point of the baffle and the aerofoil is to solve both simultaneously. However, the top and bottom aerofoils are stored as a piecewise third-degree spline. Hence, the equation for the baffle intersection point must be solved simultaneously with each segment of the spline and the derived intersection point would have to be crosschecked to lie within the upper and lower bounds of
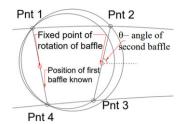
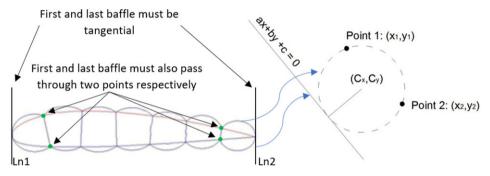**Figure C.1.** *Calculation of second baffle angle.*

Figure C.2. *Circle drawn from two points and a tangential line.*

the concerned spline segment. This iterative procedure can be replaced by a binary search algorithm, to evaluate the coordinates of the intersection points within a desired level of accuracy.

Calculating circle centre coordinates and radius given three points

Let the three available points that the circle passes through be (x_1, y_1), (x_2, y_2), (x_3, y_3). The circle centre coordinates (C_x, C_y) and radius 'r' are unknown. Substituting the three given coordinates into the equation of a circle and rearranging the terms of the three equations generated in matrix form:

$$\begin{bmatrix} 2x_1 2y_1 1 \\ 2x_2 2y_2 1 \\ 2x_3 2y_3 1 \end{bmatrix} \begin{bmatrix} C_x \\ C_y \\ r^2 - C_x^2 - C_y^2 \end{bmatrix} = \begin{bmatrix} x_1^2 + y_1^2 \\ x_2^2 + y_2^2 \\ x_3^2 + y_3^2 \end{bmatrix} \tag{C1}$$

The circle centre coordinates, and their radii can be calculated by solving Equation (C1). Subsequent baffle angles can be calculated once the first baffle angle is set.

Once the first baffle angle is fixed and the intersection points are found, the subsequent baffle angles can be calculated in a sequential manner. In each step, the left baffle becomes the known and the right baffle angle needs to be calculated. Referring Fig. C.1 two circles are drawn, one passes through points 1, 4 and 2 and the other passes through point 1, 4 and 3. Equation (C1) is used to calculate the radii given the set of three points. For all four points to pass through the same circle, these radii must be equal. Hence the angle of the second baffle is varied to minimise the difference between the two radii. The process is then repeated for the next air beam.

Start and end baffle calculations

The creation of the first and last baffle arcs involves arc creation through two fixed points and a tangent to ensure that the generated aerofoil maintains a chord of one unit as in the original smooth.

The centre coordinates and radii for the first and last compartment were derived as follows:

To avoid a case-specific derivation, the circle needs to pass through two arbitrary points marked as point 1 and point 2 having coordinates as (x_1, y_1) and (x_2, y_2), respectively, and be tangential to the line marked with the equation $ax + by + c = 0$.

The equation of the circle with respect to the first fixed point is:

$$(x_1 - C_x)^2 + (y_1 - C_y)^2 = r^2 \tag{C2}$$

Similarly with respect to the second fixed point:

$$(x_2 - C_x)^2 + (y_2 - C_y)^2 = r^2 \tag{C3}$$

The equation of the circle with respect to the line is:

$$r^2 = \frac{(aC_x + bC_y + c)^2}{a^2 + b^2} \tag{C4}$$

Substituting Equation (C4) in Equations (C2) and (C3) separately, the following two equations are generated:

$$(b^2)\,(C_x{}^2) + (-2ab)\,(C_xC_y) + (-2x_1\,(a^2 + b^2) - 2ac)\,(C_x) + (a^2)\,(C_y{}^2) \tag{C5}$$
$$+ (-2y_1\,(a^2 + b^2) - 2bc)\,(C_y) + ((a^2 + b^2)\,(x_1{}^2 + y_1{}^2) - c^2) = 0$$

$$(b^2)\,(C_x{}^2) + (-2ab)\,(C_xC_y) + (-2x_2\,(a^2 + b^2) - 2ac)\,(C_x) + (a^2)\,(C_y{}^2) \tag{C6}$$
$$+ (-2y_2\,(a^2 + b^2) - 2bc)\,(C_y) + ((a^2 + b^2)\,(x_2{}^2 + y_2{}^2) - c^2) = 0$$

Equations (C5) and (C6) are conic sections in C_x and C_y. Two intersecting conic sections have four roots, which may be all real or a mix of real and imaginary. The following steps describe the method to get the four roots and identifying the single root that resembles our arc centre.

Equations (C5) and (C6) can be written in the quadratic form of either C_x or C_y. Writing only Equation (C5) in the form of C_x,

$$(a_1)\,C_x{}^2 + (b_1C_y + c_1)\,C_x + (d_1C_y{}^2 + e_1C_y + f_1) = 0 \tag{C7}$$

Here,

$$a_1 = b^2$$

$$b_1 = -2ab$$

$$c_1 = (-2x_1\,(a^2 + b^2) - 2ac)$$

$$d_1 = a^2$$

$$e_1 = (-2y_1\,(a^2 + b^2) - 2bc)$$

$$f_1 = ((a^2 + b^2)\,(x_1{}^2 + y_1{}^2) - c^2)$$

Similarly, re-writing Equation (C6) in quadratic form of C_x

$$(a_2)\,C_x{}^2 + (b_2C_y + c_2)\,C_x + (d_2C_y{}^2 + e_2C_y + f_2) = 0 \tag{C8}$$

The solutions of the quadratic Equations (C9) and (C10) are

$$C_x = \frac{-(b_1C_y + c_1) \pm \sqrt{(b_1C_y + c_1)^2 - 4\,(a_1)\,(d_1C_y{}^2 + e_1C_y + f_1)}}{2a_1} \tag{C9}$$

$$C_x = \frac{-(b_2 C_y + c_2) \pm \sqrt{(b_2 C_y + c_2)^2 - 4(a_2)(d_2 C_y^2 + e_2 C_y + f_2)}}{2a_2} \tag{C10}$$

Equating Equations (C9) and (C10) and through manipulation of coefficients, a fourth order polynomial is derived as follows:

$$(P^2 - S) C_y^4 + (2PQ - T) C_y^3 + (Q^2 + 2PR - U) C_y^2 + (2QR - V) C_y + (R^2 - W) \tag{C11}$$

Here,

$$P = A - C_1 - C_2 \qquad\qquad\qquad T = 4(C_1 D_2 + C_2 D_1)$$
$$Q = B - D_1 - D_2 \qquad\qquad\qquad U = 4(C_1 E_2 + D_1 D_2 + E_1 C_2)$$
$$R = G - E_1 - E_2 \qquad\qquad\qquad V = 4(D_1 E_2 + E_1 D_2)$$
$$S = 4C_1 C_2 \qquad\qquad\qquad W = 4(E_1 E_2)$$

Further, all the variables in the RHS are defined as

$$A = \frac{b_1^2}{4a_1^2} - \frac{b_2^2}{4a_2^2} - \frac{b_1 b_2}{2b_1 b_2} \qquad\qquad B = \frac{b_1 c_1}{2a_1^2} - \frac{b_2 c_2}{2a_2^2} - \frac{b_1 c_2 + b_2 c_1}{2a_1 a_2}$$

$$G = \frac{c_1^2}{4a_1^2} - \frac{c_2^2}{4a_2^2} - \frac{c_1 c_2}{2a_1 a_2}$$

$$C_1 = \frac{b_1^2 - 4a_1 d_1}{4a_1^2} \qquad\qquad\qquad C_2 = \frac{b_2^2 - 4a_2 d_2}{4a_2^2}$$

$$D_1 = \frac{2b_1 c_1 - 4a_1 e_1}{4a_1^2} \qquad\qquad\qquad D_2 = \frac{2b_2 c_2 - 4a_2 e_2}{4a_2^2}$$

$$E_1 = \frac{c_1^2 - 4a_1 f_1}{4a_1^2} \qquad\qquad\qquad E_2 = \frac{c_2^2 - 4a_2 f_2}{4a_2^2}$$

Upon solving Equation (C11) to find the roots, it was found that the coefficients of the third and fourth order terms of the polynomials were zero. Hence two options of C_y are calculated. Plugging these options into Equations (C9) and (C10) would give rise to two repeated roots. These are then used to calculate two options of radii. The algorithm then chooses the option with the smaller radii and finalises the circle centre coordinates C_x and C_y.

Appendix D

This appendix elaborates the method to generate any internally baffled inflatable aerofoil.

Generating top and bottom aerofoil splines

The aerofoil spline is fitted to a single high order polynomial as compared to using a piece wise cubic spline, since the computation time to create a single inflatable aerofoil reduces. The benefit of the same is felt while running optimisation solvers as described in Section 8. The polynomial chosen to represent the upper and lower side of the aerofoil separately is:

$$y = ax^{1/3} + bx^{1/2} + cx^2 + dx^3 + ex^4 + fx^5 \tag{D1}$$

Here a to f' are the coefficients of the polynomial.

Finding circle y-coordinate of centre given x-coordinate of centre

The circle centre *x*-coordinate and top and bottom aerofoil equations are known. The outputs are circle centre *y*-coordinate and radius. Fibonacci minimisation has been used as:

$$Minimise \ J\left(C_y\right) = (T_1 - T_2)^2 \tag{D2}$$

subject to, $0 < C_y < 1$

Here,

$T_1\left(C_y\right)$ = Tangential distance between circle centre and upper aerofoil
$T_2\left(C_y\right)$ = Tangential distance between circle centre and lower aerofoil

This method to find the circle centre *y*-coordinate is time consuming because any optimisation tool-box calls the aerofoil generation algorithm. Optimisation tools used to optimise the geometry usually use non-traditional optimisation algorithms like genetic algorithms or particle swarm optimisation since the nature of the objective function space (multiple minima or single minima) is not known. This results in prohibitively high computational times to complete the analysis. To reduce the computation time, instead of calculating the circle centre *y*-coordinate each time through this iterative process, a higher order polynomial can be used that fits the radius and circle centre *y*-coordinate as a function of circle centre *x*-coordinate. The input points to fit the polynomial are generated only once at the beginning using regression, hence saving computation time.

Determining parameters of the last circle

Given that the chord length of the internally inflatable aerofoil is always less than the actual aerofoil, the user can specify the chord as a percent of the original aerofoil chord. For the results presented in this study, the inflatable aerofoil chord is taken as 90% of the original aerofoil chord. The closer the inflatable aerofoil chord is to the original aerofoil chord, the smaller is the final circle radius. Hence the user can select the chord based on the manufacturing capabilities available.

Choosing the parameters of the first circle

The *x*-coordinate of the centre of the first circle can be chosen by the user, which depends on the manufacturing capabilities available. In this study, the *x*-coordinate of the first circle is 0.04 units where the original aerofoil chord is one unit.

Finding the circle data for the remaining circles

Once the centre coordinates of first and last circle are fixed, the *x*-coordinates of the remaining circle centres are equally spaced depending on the number of compartments the user has specified. The *y*-coordinates of the circle centres and their radii are calculated using the method illustrated in previous subsection.

This process illustrates the entire method to create an internally baffled aerofoil. Finally, the ACR is calculated, and all the circle centre coordinates and radii are given to the user for further processing. An example of using this methodology is illustrated in the next section.